J. Fluid Mech. (2007), *vol.* 574, *pp.* 429–448. © 2007 Cambridge University Press
doi:10.1017/S0022112006004265 Printed in the United Kingdom

Coherent vortices and tracer cascades in two-dimensional turbulence

ARMANDO BABIANO[1] AND ANTONELLO PROVENZALE[2]

[1]Laboratoire de Météorologie Dynamique, Département de Géophysique de l'ENS de Paris, 24, rue Lhomond, 75005, Paris, France
babiano@lmd.ens.fr

[2]Istituto di Scienze dell'Atmosfera e del Clima, CNR, Corso Fiume 4, 10133 Torino, Italy
a.provenzale@isac.cnr.it

(Received 12 July 2006 and in revised form 10 October 2006)

We study numerically the scale-to-scale transfers of enstrophy and passive-tracer variance in two-dimensional turbulence, and show that these transfers display significant differences in the inertial range of the enstrophy cascade. While passive-tracer variance always cascades towards small scales, enstrophy is characterized by the simultaneous presence of a direct cascade in hyperbolic regions and of an inverse cascade in elliptic regions. The inverse enstrophy cascade is particularly intense in clusters of small-scales elliptic patches and vorticity filaments in the turbulent background, and it is associated with gradient-decreasing processes. The inversion of the enstrophy cascade, already noticed by Ohkitani (Phys. Fluids A, vol. 3, 1991, p. 1598), appears to be the main difference between vorticity and passive-tracer dynamics in incompressible two-dimensional turbulence.

1. Introduction

The dynamics of forced and dissipated two-dimensional incompressible flows is described by the vorticity equation,

$$\frac{\partial \omega}{\partial t} + u\frac{\partial \omega}{\partial x} + v\frac{\partial \omega}{\partial y} = F + D, \tag{1.1}$$

where $\omega \equiv \partial v/\partial x - \partial u/\partial y$ is relative vorticity, $\boldsymbol{u} \equiv (u, v)$ is the fluid velocity, (x, y) are spatial coordinates, t is time, and F and D represent forcing (vorticity sources) and dissipation (vorticity sinks) respectively. Formally, the evolution of the concentration of a passive-scalar tracer, θ, is described by the same equation that governs vorticity dynamics. Unlike the linear advection of a passive tracer, however, the dynamics of vorticity is strongly nonlinear as the fluid velocity $\boldsymbol{u}$ and vorticity ω are related to each other. This makes vorticity an active tracer, i.e. a tracer that feeds back on the advecting velocity field. Owing to this relationship, when forcing and dissipation are absent there are two quadratic invariants for vorticity ω (energy, $E = (1/2L^2)\int(u^2 + v^2)\,\mathrm{d}x\,\mathrm{d}y$ and enstrophy, $Z = (1/2L^2)\int \omega^2\,\mathrm{d}x\,\mathrm{d}y$, where L is the domain size), while there is just one quadratic invariant for a passive tracer θ (the variance of the tracer concentration, $\Theta = (1/2L^2)\int \theta^2\,\mathrm{d}x\,\mathrm{d}y$). This leads to fundamentally different dynamical properties for apparently identical evolution equations (Babiano *et al.* 1987).

One important consequence of the difference between vorticity and passive tracers is the ability of vorticity to self-organize into coherent vortices (McWilliams 1984, 1990; Bracco *et al.* 2000*b*). In a sense, the problem of two-dimensional turbulence lies in the self-organization of intense, spatially localized coherent vorticity concentrations that induce strong correlations in the Fourier phases and make the turbulent field dynamically inhomogeneous. Vortices have long-range effects and their influence extends well into the background turbulence, largely determining its properties (Bracco *et al.* 2000*a*; Pasquero, Provenzale & Babiano 2001; Elhmaidi, von Hardenberg & Provenzale 2005).

Because velocity and passive-tracer concentration are not related to each other, the above mechanism is absent in passive-tracer dynamics. However, if the vorticity and the passive-tracer fields initially coincide, then both the enstrophy and passive-tracer variance spectra evolve in the same way, since the initial correlation persists at all times owing to the linearity of passive advection. If vorticity and passive tracer are initially uncorrelated and the sources of enstrophy and scalar variance are kept uncorrelated, then the absence of correlation persists at all times. In this case, numerical simulations indicate that the slope of the enstrophy spectrum $Z_\omega(k)$ is usually steeper that the Batchelor–Kraichnan (B-K) prediction k^{-1}, owing to the presence of coherent vortices. Conversely, the passive-tracer variance spectrum $Z_\theta(k)$ obeys the k^{-1} regime (Batchelor 1959; Kraichnan 1967; Batchelor 1969). When the coherent vortices are artificially destroyed, the enstrophy spectrum becomes similar to that of the passive tracer and both obey the k^{-1} self-similarity behaviour (Babiano *et al.* 1987).

Careful numerical explorations have shown that the main differences between vorticity and passive-tracer spectral-transfer fluxes take place in elliptic (vorticity-dominated) regions (Babiano *et al.* 1987; Ohkitani 1991). These works suggested that elliptic regions, related to the presence of coherent vortices, can affect the cascades of enstrophy and passive-tracer variance in ways that are overlooked by standard similarity theories.

The difference between active (vorticity) and passive tracer dynamics has been further investigated by looking at the geometrical alignment of tracer gradients. In two-dimensional turbulence, Protas, Babiano & Kevlahan (1999) numerically confirmed that the production of vorticity gradients by stirring depends on the relative orientation between the gradient itself and the compressional axis of the rate-of-strain tensor (Weiss 1991). Kimura & Herring (2001) studied vortex filament ejection following the gradient enhancement process for vorticity. More detailed studies have considered both vorticity and passive scalars (Lapeyre, Klein & Hua 1999; Klein, Hua & Lapeyre 2000), and argued that the value of the Lagrangian derivative of the tracer-gradient variance, which is related to the alignment process and to the efficiency of the direct tracer-variance cascade, can be used as an indicator to distinguish vorticity from passive tracers.

Later studies, however, raised questions on the existence of significant differences in gradient alignment properties of active and passive tracers. The numerical analyses discussed by Lapeyre, Hua & Klein (2001) showed that even though transient differences are observed in the early stages of enstrophy and tracer-variance cascades, the diagnostics based on the cascade efficiency cannot distinguish between passive scalars and vorticity when turbulence is fully developed. Similar results are found when considering either global averages or conditional averages restricted to elliptic or hyperbolic regions in terms of the Okubo–Weiss (O-W) or Hua–Klein flow segmentation criteria (Okubo 1970; Weiss 1991; Hua & Klein 1998). Dubos & Babiano (2003) revisited this problem using conditional averages and considering the Lagrangian derivative of the cascade efficiency, i.e. the second Lagrangian derivative of the tracer-gradient variance. Also in this case, the conclusion was that the enstrophy and passive-tracer variance cascades seem to be very similar to each other.

The results reported above indicate an apparent inconsistency in our understanding of vorticity and passive-tracer dynamics in vortex-dominated flows. On one hand, when either initial or source-generated correlations between vorticity and passive scalars are absent, the global spectra of enstrophy and passive-tracer variance are significantly different. On the other hand, the overall local properties of the turbulent cascades, as measured by tracer-gradient dynamics and orientation, seem quite similar.

A first observation is that tracer-gradient dynamics captures only small-scale processes, and thus provides an incomplete picture of the transfer processes in the inertial range. This is particularly important in two-dimensional flows where the coherent vortices destroy the self-similarity and the dynamical homogeneity of transfer dynamics (Babiano & Dubos 2005). Owing to the presence of coherent structures, the dynamical transfers at intermediate scales in the inertial range do not behave as expected from similarity theory. The purpose of the present contribution is to revisit this question from a point of view that unifies small-scale analyses based on gradient dynamics with diagnostics that are in principle sensitive to the dynamics in the whole inertial range. We focus on the effective difference between vorticity and passive tracers in terms of energy and enstrophy transfers at scales that are larger than those captured by gradient dynamics.

2. Two-dimensional tracer-cascade diagnostics

2.1. *Equations of motion*

In the absence of energy sources and sinks and neglecting molecular diffusivity, the evolution equations for a scalar T and its gradient, $\boldsymbol{q} = \nabla T$, in a two-dimensional incompressible flow are written as

$$\frac{\partial T}{\partial t} + \boldsymbol{u}\cdot\boldsymbol{q} = 0, \tag{2.1}$$

$$\frac{\mathrm{d}}{\mathrm{d}t}\boldsymbol{q} + \boldsymbol{A}^{*}\boldsymbol{q} = 0, \tag{2.2}$$

where

$$\boldsymbol{A}^{*} = \frac{1}{2}\begin{bmatrix} s_1 & s_2+\omega \\ s_2-\omega & -s_1 \end{bmatrix}$$

denotes the transpose of the velocity-gradient matrix $\boldsymbol{A}$,

$$s_1 = -2\frac{\partial v}{\partial y} \quad \text{and} \quad s_2 = \frac{\partial v}{\partial x} + \frac{\partial u}{\partial y}.$$

Equations (2.1) and (2.2) are linear if $T = \theta$ and nonlinear if $T = \omega$.

In the case of vorticity, equation (2.2) cannot be solved analytically owing to the dependence of ω, s_1 and s_2 on fluid velocity. In the case of a passive tracer, the only difficulty in solving the linear problem (2.2) comes from the time dependence of $\boldsymbol{A}^{*}$. If we assume that the temporal evolution of $\boldsymbol{A}^{*}$ is slow compared to that of $\boldsymbol{q}$, we can approximate equation (2.2) with an eigenvalue problem. The behaviour of $\boldsymbol{q}$ then depends on whether the transpose of the velocity gradient has real or imaginary eigenvalues. This is determined by the sign of the O-W (Okubo–Weiss) parameter

$$Q = s_1^2 + s_2^2 - \omega^2. \tag{2.3}$$

The sign of the O-W parameter (2.3) quantifies the topology of two-dimensional turbulence and it divides the turbulent flow into two different dynamical regions: elliptic regions where $Q < 0$, the eigenvalues are purely imaginary and tracer gradients are expected to rotate without growing or decreasing; and hyperbolic regions where $Q > 0$ (two real and opposite eigenvalues) and gradients grow exponentially. In hyperbolic regions, tracer gradients are expected to align with the eigenvector of maximum compression (Weiss 1991). Limitations of the O-W approach have been discussed by Basdevant & Philipovitch (1994) and an extension based on considering the eigenvalues of the acceleration-gradient tensor (the Hessian of pressure) has been proposed by Hua & Klein (1998). On the other hand, the O-W parameter (2.3) is a quantity that can be easily estimated, and it has a close relationship with the Laplacian of pressure, $Q = -4\nabla^2 p$ (Larcheveque 1993). For this reason, as well as for consistency with previous work (Ohkitani 1991) and recent analyses of the inverse energy cascade (Babiano & Dubos 2005), here we characterize the topology of two-dimensional turbulence using the standard O-W parameter (2.3).

2.2. *Cascade efficiency*

The temporal evolution of tracer gradient, $\boldsymbol{q}$, is determined by the rate-of-strain tensor, $\boldsymbol{S} = \frac{1}{2}(\boldsymbol{A} + \boldsymbol{A}^*)$, which intensifies the gradient, and by vorticity, which rotates the gradient direction. Using this decomposition, from (2.2) one can derive a local indicator of the efficiency of the tracer cascade, measuring the production or destruction of tracer-gradient variance:

$$\sigma \equiv \frac{\mathrm{d}}{\mathrm{d}t} q^2 = -2\boldsymbol{q}^* \cdot \boldsymbol{S} \cdot \boldsymbol{q}. \tag{2.4}$$

The above equation shows that the production or destruction of tracer-gradient variance depends on the angle between the tracer gradient and the compressional axis of the rate-of-strain tensor $\boldsymbol{S}$. The physical interpretation of σ in terms of a cascade is simple: a positive value of σ indicates growth of gradient amplitude and an intensification of the direct tracer cascade. Effective gradient production occurs in hyperbolic regions, where $Q > 0$, whereas σ remains approximately zero in elliptic domains where $Q < 0$. This behaviour has been clearly demonstrated by Klein *et al.* (2000), using the concept of effective rotation (i.e. the rotation due both to vorticity and to the rotation of the principal axes of the rate-of-strain tensor). However, those results also indicated that the mean value of σ in elliptic domains can be positive. Further analyses by Lapeyre *et al.* (2001) and Dubos & Babiano (2003) showed that the mean value of σ vanishes in strong elliptic regions, but it can be significantly larger than zero in weak elliptic regions, for either vorticity or passive tracers. This behaviour is consistent with the presence of direct cascades of passive-tracer variance and of enstrophy in elliptic regions.

The above results raise the question of whether a negative cascade efficiency, which characterizes small-scale gradient-decreasing structures, has any dynamical significance in the vorticity/passive-tracer problem. In the numerical investigations that follow, we explore this issue and focus on the sign of first-order diagnostics (2.4) to perform conditional statistics based on (2.3). To illustrate some of the dynamical quantities that will be analysed in the following, in figure 1 we show two snapshots of the instantaneous spatial distribution of cascade efficiency, σ, for vorticity (*a*) and passive-tracer (*b*) variances. Operationally, the cascade efficiency is computed as $\sigma = -2\boldsymbol{q}^* \cdot \boldsymbol{S} \cdot \boldsymbol{q}$ from the results of the numerical simulations analysed in the present work.

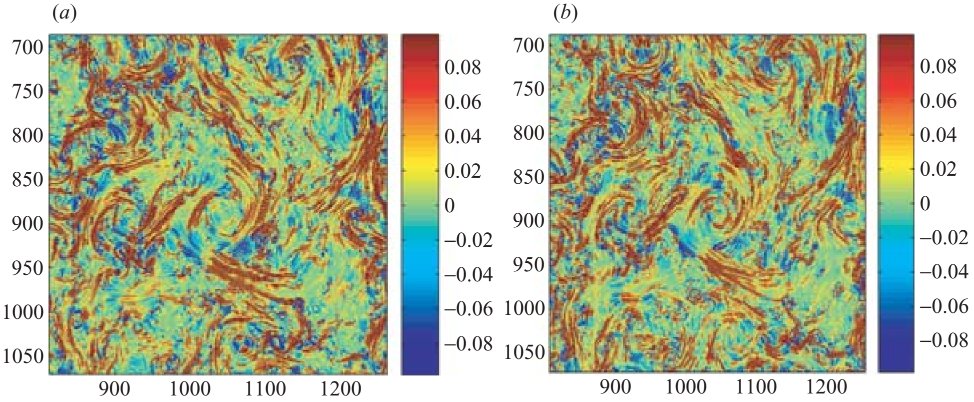

FIGURE 1. Instantaneous spatial distribution of the cascade efficiencies, σ, for vorticity (*a*) and passive-tracer (*b*) variances.

2.3. *Transfer of tracer variance on larger scales*

The cascade efficiency (2.4) is based on gradient dynamics and it unambiguously captures the local transfer properties at the smallest length scales. However, the definition of σ does not carry information on the character of the cascade on larger length scales. To explore what happens on larger scales, we resort to the use of statistics based on two-point tracer increments (Dubos & Babiano 2002). In a cascade process, the contribution of structures at length scale l is traditionally determined by looking at the magnitude of increments over the spatial separation l. The tracer increment $\delta T(\boldsymbol{x}, \boldsymbol{l})$ at the position $\boldsymbol{x}$ in physical space is defined as $\delta T(\boldsymbol{x}, \boldsymbol{l}) = T(\boldsymbol{x} + \boldsymbol{l}/2) - T(\boldsymbol{x} - \boldsymbol{l}/2)$, and its magnitude is measured by δT^2. Both quantities are functions of the independent (vector) variables $\boldsymbol{x}$ and $\boldsymbol{l}$ and they obey an advection equation such as (2.1), with advection provided by the velocity increment $\delta \boldsymbol{u}(\boldsymbol{x}, \boldsymbol{l})$, defined analogously to $\delta T(\boldsymbol{x}, \boldsymbol{l})$.

Using incompressibility and the independence of $\boldsymbol{x}$ and $\boldsymbol{l}$, Dubos & Babiano (2002) showed that in the inviscid case the budget of tracer variance as a function of $\boldsymbol{x}$ and $l = \| \boldsymbol{l} \|$ is governed by the equation

$$\frac{\partial}{\partial t} \oint \delta T^2 \frac{\mathrm{d}\phi}{2\pi} + \nabla_x \cdot \oint \delta T^2 U \frac{\mathrm{d}\phi}{2\pi} + \frac{\partial}{l \partial l} l \oint \delta T^2 \delta u_\parallel \frac{\mathrm{d}\phi}{2\pi} = 0, \tag{2.5}$$

where ϕ is the polar angle of $\boldsymbol{l}$, $\delta u_\parallel = \delta \boldsymbol{u}(\boldsymbol{x}, \boldsymbol{l}) \cdot \boldsymbol{l}/l$ denotes the longitudinal velocity increment, ∇_x is the gradient operator with respect to $\boldsymbol{x}$ and U is the velocity averaged over the positions $(\boldsymbol{x} + \boldsymbol{l}/2)$ and $(\boldsymbol{x} - \boldsymbol{l}/2)$.

The time evolution in (2.5) is due to the sum of two contributions: transport in physical space with velocity U (second term) and scale-to-scale transfer with velocity $\delta u_\parallel(\boldsymbol{x}, \boldsymbol{l})$ (third term). We focus on the latter term, and define the flux of tracer variance (taken positive from large to small scales)

$$F(\boldsymbol{x}, t; l) = -\frac{1}{2l} \langle \delta T^2 \delta u_\parallel \rangle_\phi = -\frac{1}{2l} \oint \delta T^2 \delta u_\parallel \frac{\mathrm{d}\phi}{2\pi}, \tag{2.6}$$

where $\langle . \rangle_\phi$ indicates an average over the angle ϕ (see Dubos & Babiano (2002) for a detailed discussion). The small-scale limit of the flux F is related to the alignment properties described by (2.4), and the Taylor expansion of (2.6) gives (Dubos &

Babiano 2002)

$$F(\boldsymbol{x}, l) \approx -\frac{l^2}{8}\boldsymbol{q}^* \cdot \mathbf{S} \cdot \boldsymbol{q} = \frac{l^2}{16}\sigma. \tag{2.7}$$

Note, however, that the full expression (2.6) holds also at larger length scales as its validity extends throughout the inertial range. The spatial average of (2.6) defines the mean tracer-transfer rate at length scale l,

$$\varepsilon_T(l) = \langle F(\boldsymbol{x}, l)\rangle. \tag{2.8}$$

For a self-similar cascade, $\varepsilon_T(l)$ must be scale-independent in the inertial range, as expected from the Kolmogorov–Batchelor–Kraichnan self-similarity theories. For comparison, see Yaglom (1949) for the derivation of an analogous expression relating the second-order moment of tracer increments to the third-order mixed moments of longitudinal velocity and tracer increments in three-dimensional turbulence.

2.4. *Enstrophy transfer rate and velocity increments*

In the inertial range of the enstrophy cascade, the mean enstrophy transfer rate ε_ω is related to the third-order moment of the distribution of velocity increments (Lindborg 1999),

$$\tfrac{1}{4} l^3 \varepsilon_\omega = \left\langle \left(\frac{\boldsymbol{l}}{l} \cdot \delta \boldsymbol{u}\right)(\delta \boldsymbol{u} \cdot \delta \boldsymbol{u}) \right\rangle = \langle \delta u_\parallel \delta u_\parallel \delta u_\parallel \rangle + \langle \delta u_\parallel \delta u_\perp \delta u_\perp \rangle \tag{2.9}$$

where the transverse velocity increment is defined as $\delta u_\perp = \delta \boldsymbol{u} \times \boldsymbol{l}/l$ and $\langle . \rangle$ indicates an average on both the polar angle ϕ and space $\boldsymbol{x}$.

Relationship (2.9) is in line with Batchelor's result for homogeneous turbulence (Batchelor 1953),

$$\nabla^2 \langle \boldsymbol{u}(\boldsymbol{x}) \cdot \boldsymbol{u}(\boldsymbol{x} + \boldsymbol{l})\rangle = -\langle \omega(\boldsymbol{x}) \omega(\boldsymbol{x} + \boldsymbol{l})\rangle \tag{2.10}$$

and it has been verified by Lindborg & Alvelius (2000). Since the averaging is performed over all angles, the third-order moments present in equation (2.9) must be independent of direction, and they fulfil the two-dimensional version of Landau's condition for isotropy (Landau & Lifshitz 1971; Lindborg 1999),

$$\langle \delta u_\parallel \delta u_\perp \delta u_\perp \rangle = \frac{l}{3} \frac{\mathrm{d}}{\mathrm{d}l} \langle \delta u_\parallel \delta u_\parallel \delta u_\parallel \rangle. \tag{2.11}$$

Relationship (2.11) was numerically confirmed in both the energy and enstrophy ranges of two-dimensional turbulence by Babiano & Dubos (2005).

Using (2.11), one finds from (2.9)

$$\langle \delta u_\parallel \delta u_\parallel \delta u_\parallel \rangle = \langle \delta u_\parallel \delta u_\perp \delta u_\perp \rangle = \tfrac{1}{8} l^3 \varepsilon_\omega, \tag{2.12}$$

which, using (2.6) and (2.8) and dividing by l^3, can be rewritten in the enstrophy inertial range as

$$\frac{1}{l^2} \frac{\langle \delta u_\parallel \delta u_\parallel \delta u_\parallel \rangle}{l} = \frac{1}{l^2} \frac{\langle \delta u_\parallel \delta u_\perp \delta u_\perp \rangle}{l} = -\frac{1}{8} \frac{\langle \delta \omega^2 \delta u_\parallel \rangle}{2l}. \tag{2.13}$$

Relation (2.13) appears as a constraint on vorticity dynamics, owing to the presence of the energy invariant, and it may be interpreted in a statistically steady enstrophy inertial range as a budget relation between the direct enstrophy transfer towards small scales ($-\langle \delta \omega^2 \delta u_\parallel \rangle / 2l$) and an inverse transfer of energy to large scales ($\langle \delta u_\parallel \delta u_\parallel \delta u_\parallel \rangle / l$ and $\langle \delta u_\parallel \delta u_\perp \delta u_\perp \rangle / l$) with a proportionality factor of $8/l^2$.

Expression (2.13) determines the relationship between the third-order moments of the tranverse and longitudinal velocity increments and the scale-to-scale transfer of vorticity variance and it depends on the existence of the relationship (2.10) between $\boldsymbol{u}$ and ω, which embodies the feedback of vorticity on velocity and the presence of the energy invariant. The energy invariant can be seen as the spatial integral of vorticity, since $\omega = \partial v/\partial x - \partial u/\partial y$. Thus, the conservation of enstrophy corresponds to the conservation of tracer variance, while the conservation of energy is unmatched in the case of a passive tracer. Owing to this difference, the results discussed above do not hold for a passive tracer θ and the scale-to-scale transfer $\langle \delta\theta^2 \delta u_{\|} \rangle / 2l$. In this case, the inverse energy cascade and the direct scale-to-scale transfer of passive-tracer variance are not related to each other.

Expression (2.13) has been derived from a global average over the entire flow domain (homogeneity assumption). The same expression does not necessarily hold in selected dynamical sub-domains of the turbulent flow, as identified by conditional averages based on the topological characteristics of the flow. For this reason, a detailed topologically conditioned analysis can provide interesting information on the local cascade structure, and it can help to assess whether the cascade properties of ω in selected sub-domains differ from the global-mean behaviour (2.13).

3. Numerical procedure

We simulate tracer dynamics in forced–dissipated two-dimensional turbulence by solving in parallel equation (2.1) for vorticity and for a passive tracer in a doubly periodic domain with size $2\pi \times 2\pi$. Forcing F (vorticity or passive-tracer source) is obtained by keeping constant the modulus of the Fourier mode at a selected wavenumber $\boldsymbol{k}_I$. Dissipation D, for both vorticity and passive tracer, is obtained as the sum of a large-scale linear friction and a small-scale dissipation. The former is given by an inverse Laplacian and the latter is given by a eighth-order iterated Laplacian (Babiano *et al.* 1987; Elhmaidi *et al.* 1993; Pasquero *et al.* 2001; Elhmaidi *et al.* 2005).

Equation (2.1) is numerically solved by a standard pseudo-spectral scheme with resolution 1728 × 1728 grid points. Initial conditions on ω and θ are provided by two independent random fields. The modulus of the forcing wavenumber is set at $k_I = (k_{x,I}^2 + k_{y,I}^2)^{1/2} = 40$. In the initialization of the passive tracer, we ensure that no initial correlation exists between θ and ω. During the numerical integration, the passive-tracer concentration θ is forced at the wavenumber $\boldsymbol{k}_I^\theta = (40, 0)$ and vorticity is forced at $\boldsymbol{k}_I^\omega = (0, 40)$. Passive-tracer concentration and vorticity are dissipated in the same way. After an initial transient, the system enters a regime of statistically stationary forced and dissipated turbulence that is the focus of the present analysis. In the statistically stationary turbulent regime, there is a well-developed direct enstrophy cascade over an extended range of scales and the correlation between ω and θ remains approximately zero (Babiano *et al.* 1987). The numerical resolution is sufficient to study both large- and small-length-scale dynamics and extends the numerical study performed long ago by Babiano *et al.* (1987), by allowing for the simultaneous presence of enstrophy and energy cascade ranges.

In the following, we analyse the outputs of the numerical simulations for ω and θ, separating the contributions of elliptic and hyperbolic domains (as defined by the O-W criterion (2.3)) to the transfer dynamics. In addition to topological selection, we occasionally refine the conditional statistics by adding a second constraint based either on the value of the squared vorticity or on the sign of the first Lagrangian derivative of the tracer-gradient variance (2.4), to identify the structures associated with gradient growth and gradient decrease. One goal is to determine whether and where there are significant local differences from the globally averaged scale-to-scale transfers. To this end, we focus on the third term in equation (2.5), and for each length scale l we analyse the distribution of the (angle-averaged) flux $F_{\omega,\theta}(\boldsymbol{x}, l)$ (2.6) and of the conditionally averaged value of $\varepsilon_{\omega,\theta}(l)$, defined by (2.8).

The O-W parameter (2.3) is normalized as $Q^* = (s_1^2 + s_2^2 - \omega^2)/(s_1^2 + s_2^2 + \omega^2)$. The quantity Q^* has the same sign as Q, but its amplitude varies between -1 and $+1$. Whenever two-point statistics are used, conditional selection is performed by imposing the selection constraint on both points. We thus define conditional mean scale-to-scale transfers $\varepsilon'_\omega(l)$ and $\varepsilon'_\theta(l)$ by averaging (2.6) over regions where $(Q^*(\boldsymbol{x} + \boldsymbol{l}/2) < 0,\ Q^*(\boldsymbol{x} - \boldsymbol{l}/2) < 0)$ for what we call 'elliptic transfers', and on regions where $(Q^*(\boldsymbol{x} + \boldsymbol{l}/2) > 0,\ Q^*(\boldsymbol{x} - \boldsymbol{l}/2) > 0)$ for 'hyperbolic transfers'. (For conditional statistics, the angle average at any given length scale l is obtained implicitly by averaging over different pairs of points with random orientations.) In addition to the one-point cascade efficiency (2.4) and its positive σ^+ $(\sigma(\boldsymbol{x}) > 0)$ or negative σ^- $(\sigma(\boldsymbol{x}) < 0)$ values, we also define the *two-point* cascade efficiencies σ_l^+ $(\sigma(\boldsymbol{x} + \boldsymbol{l}/2) > 0, \sigma(\boldsymbol{x} - \boldsymbol{l}/2) > 0)$ and σ_l^- $(\sigma(\boldsymbol{x} + \boldsymbol{l}/2) < 0, \sigma(\boldsymbol{x} - \boldsymbol{l}/2) < 0)$, in order to select dynamical regions associated with gradient growth or gradient decrease as a function of length scale l. Analogously, we analyse the third-order moments of velocity increments entering (2.9)–(2.13) and the second-order vorticity and passive-tracer structure functions which define the corresponding spectra.

4. Properties of the tracer cascades

4.1. *Spectra and global spectral fluxes*

Panels (*a*) and (*b*) of figure 2 show the tracer variance spectra $Z_{\omega,\theta}(k)$ and the global spectral fluxes $\Phi_{\omega,\theta}(k)$ as a function of the radial wavenumber $k \equiv (k_x^2 + k_y^2)^{1/2}$, in the statistically stationary turbulent regime. The wavenumber has been normalized by the forcing wavenumber k_I. In panel (*a*) we show the compensated spectra, obtained by multiplying the spectra by the wavenumber k. The B-K regime k^{-1} would thus correspond to a flat spectral plateau.

The enstrophy and passive-tracer variance spectra behave similarly when k/k_I is sufficiently large. At smaller wavenumbers, the two spectra differ significantly from each other. For wavenumbers k/k_I less than about 5, the compensated passive-tracer variance spectrum displays an approximate plateau, consistent with a direct tracer cascade in the B-K sense. By contrast, the enstrophy spectrum is steeper than the B-K prediction, as often observed in numerical simulations where strong coherent vortices are present. According to Babiano *et al.* (1987), localness in physical space, associated with energy conservation and the formation of coherent vortices, is responsible for enstrophy spectral slopes larger than -1. No coherent vortices spontaneously form in the passive-tracer distribution, and thus the passive-tracer spectrum remains closer to the B-K prediction k^{-1}. Figure 2(*b*) shows that the global spectral fluxes are positive for $k/k_I > 1$, consistent with the direct cascade of enstrophy and passive-tracer variance. Here, both vorticity and passive-tracer fluxes display approximately constant plateaux. The average value of the passive-tracer spectral flux at the plateau, Φ_θ^0, is slightly larger than that of vorticity, Φ_ω^0. This small difference is, in fact, very important, as will be seen from the following analysis.

For $k/k_I < 1$, the enstrophy spectrum is dominated by the inverse cascade of energy. Since there is no energy invariant for the passive tracer, no inverse cascade is present in that case. As a result, the spectral density at $k/k_I < 1$ is significantly lower for passive tracer than for vorticity.

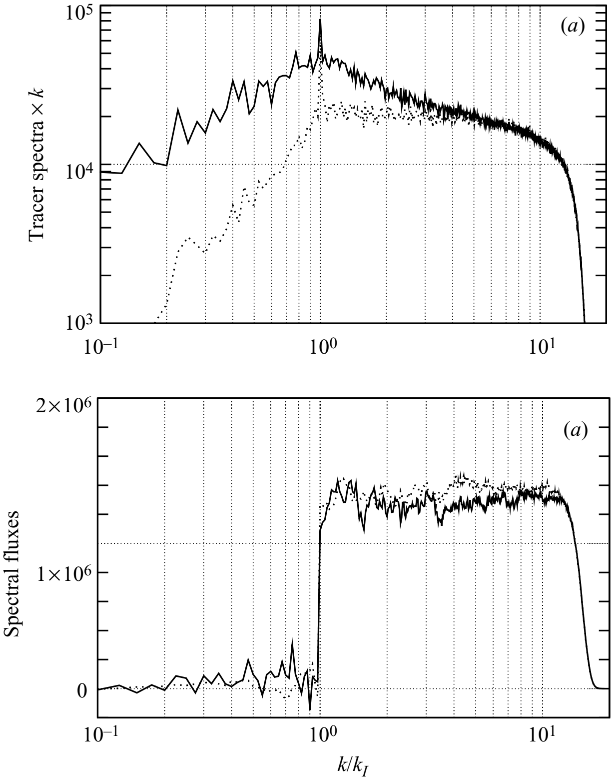

FIGURE 2. (*a*) tracer spectra compensated by k^{-1}; (*b*) tracer spectral fluxes. Spectra and spectral fluxes are not normalized. Vorticity is indicated by continuous lines and passive tracer by dotted lines.

Tracer-variance spectra are the Fourier transform of the second-order moments of tracer increments, $\langle \delta T^2(\boldsymbol{x}, \boldsymbol{l})\rangle$, also called the structure functions. Figure 3 shows the vorticity and passive-tracer structure functions as a function of length scale, when the spatial average is taken either on the entire flow domain or by excluding from the averaging procedure all 'elliptic' increments where $Q^* < 0$ at both $\boldsymbol{x} - \boldsymbol{l}/2$ and $\boldsymbol{x} + \boldsymbol{l}/2$. The length scale is normalized by l_I, where l_I is the energy injection scale ($l_I = \pi/k_I$). Vorticity (circles) and passive-tracer (triangles) structure functions are different when averaged over the whole domain, but they become similar to each other when the average excludes elliptic regions. This confirms that the main differences between vorticity and passive-tracer dynamics are found in elliptic regions, while vorticity in hyperbolic regions around and between vortices behaves approximately as a passive tracer. The behaviour of the structure functions quantitatively confirms previous results obtained with a cruder clipping technique (Babiano *et al.* 1987).

4.2. *Elliptic tracer transfers*

Figure 4 shows the scale-to-scale elliptic tracer transfers, $\varepsilon'_{\omega,\theta}$, as a function of length scale, obtained by the conditional averaging procedure discussed in §3. For comparison, we also show the elliptic transfers in the case of random fields used as initial conditions. Transfers are normalized by $(\Phi^0_\omega + \Phi^0_\theta)/2$. As expected, elliptic transfers are approximately zero for the random fields (small circles and triangles). In the fully developed turbulent regime, the elliptic transfers for vorticity and passive

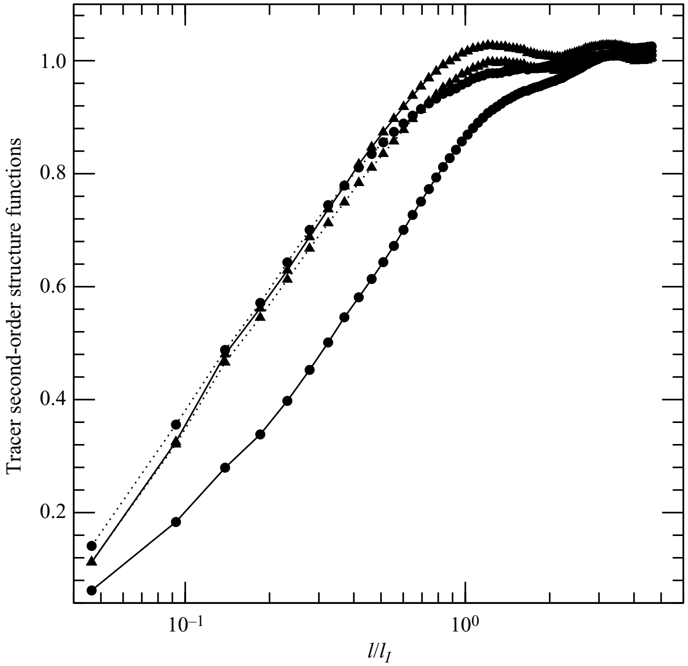

FIGURE 3. Second-order structure functions versus length scale. Circles indicate vorticity and triangles indicate passive tracer. Global averages are indicated by filled symbols while open symbols indicate conditional averages obtained by excluding elliptic two-point increments. Structure functions for vorticity are normalized by the total enstrophy, while those for passive tracer are normalized by the total scalar variance. At small scales, the structure functions grow quadratically as a function of scale.

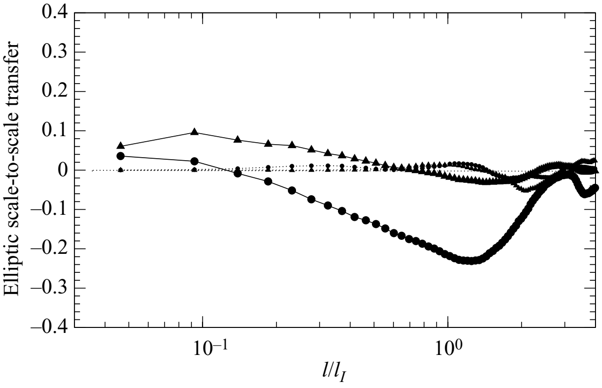

FIGURE 4. Elliptic scale-to-scale tracer transfers as a function of the length scale, for vorticity (large circles), passive tracer (large triangles), and for the corresponding random fields used as initial conditions (small circles and triangles).

tracer, ε'_ω and ε'_θ, behave very differently from each other. While the elliptic enstrophy transfer ε'_ω is negative in the whole enstrophy inertial range (except at very small scales), the passive-scalar transfer in elliptic regions, ε'_θ, is small and slightly positive. As discussed above, a positive value of $\langle F(\boldsymbol{x}, l)\rangle$ (see (2.8) and (2.5)–(2.6)) implies a direct cascade from large to small scales, and a negative value of $\langle F(\boldsymbol{x}, l)\rangle$ is

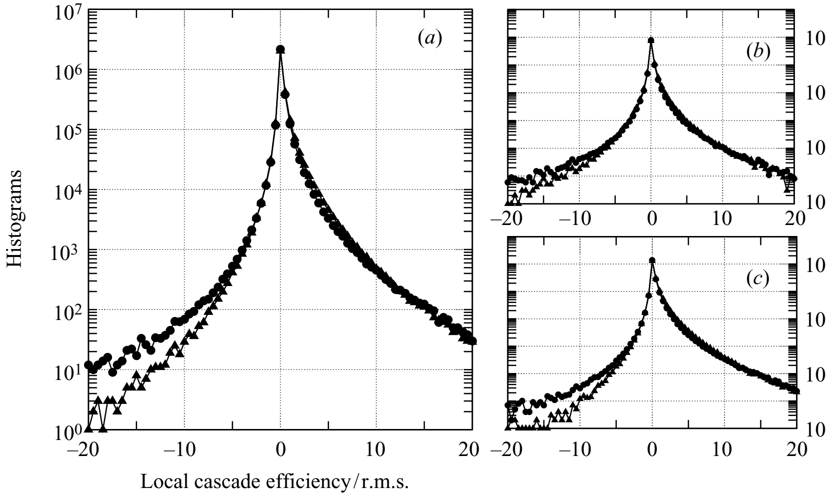

FIGURE 5. Histograms of tracer cascade efficiency, σ, for vorticity (circles), passive tracer (triangles): (*a*) unconditioned statistics, (*b*) $Q^* < 0$ and (*c*) $Q^* > 0$. The local cascade efficiencies are normalized by their r.m.s. value.

associated with an inverse cascade from small to large scales. Thus, in the scale range of the (global) direct enstrophy cascade, enstrophy and passive-tracer variance seem to undergo different cascade processes. In elliptic domains, passive-tracer variance goes from large to small length scales whereas enstrophy goes from small to large length scales. That is, in elliptic domains the enstrophy cascade is reversed with respect to the global (direct) cascade.

The inversion of the enstrophy cascade is a clear illustration of the departure from the B-K theory. Such an inversion is consistent with the steeper slope of the enstrophy spectral density in the wavenumber range $1 < k/k_I < 5$, compared to the passive-tracer spectral density which displays a k^{-1} behaviour in the same spectral range (figure 2*a*). It is important to emphasize that both ε'_ω and ε'_θ are positive at very small scales, consistent with a direct cascade at the smallest scales in elliptic domains also. This implies a positive value of σ, as defined by (2.4), and growth of gradients close to the dissipative length scales (Lapeyre *et al.* 2001; Dubos & Babiano 2003).

4.3. *Probability distribution of local tracer transfers at small scales*

The small-scale properties of tracer transfers are captured by the one-point cascade efficiency, σ, defined in (2.4) and in practice computed by finite differences at the grid spacing, Δx. Figure 5 shows the histograms of σ computed in the whole domain (*a*) as well as only in elliptic (*b*) and hyperbolic (*c*) regions. The global histogram of the cascade efficiency is peaked at $\sigma = 0$, but it is asymmetric with positive average, consistent with forward enstrophy and tracer-variance cascades. Note, however, that the probability of occurrence of negative σ values is larger for vorticity (circles) than for passive tracer (triangles). The same picture is observed in elliptic (*b*) and hyperbolic (*c*) domains. The higher efficiency of direct passive-tracer transfers, compared to vorticity transfers, has been discussed in previous studies, see e.g. Holloway & Krismannsson (1984) and Lesieur & Herring (1985). The form of the histograms shown in figure 5 confirms this and indicates that the main differences between vorticity and passive-tracer dynamics arise from gradient-decreasing processes associated with negative σ values. In any case, these differences

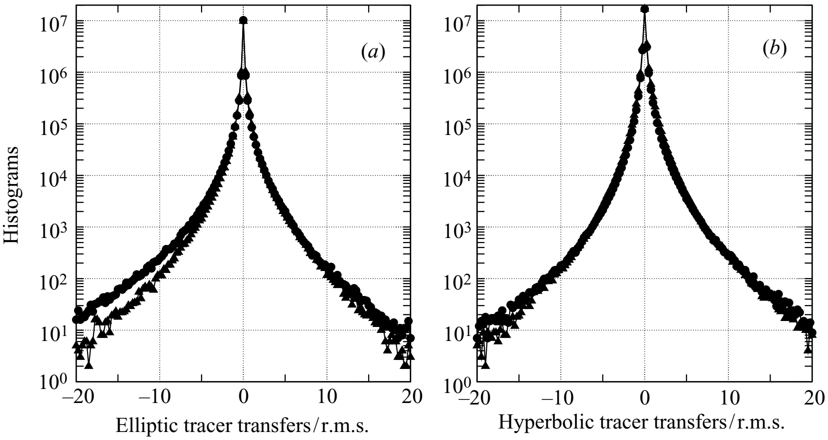

FIGURE 6. Histograms of tracer transfers, $F(\boldsymbol{x}, l)$ for vorticity (circles) and passive tracer (triangles): (*a*) $Q^* < 0$, (*b*) $Q^* > 0$. In all cases, $l/l_I = 0.3$. The tracer transfers are normalized by their r.m.s. value.

are not large enough to change the positive average of the histogram even in elliptic domains (figure 5*b*). This is consistent with the fact that the elliptic transfers, $\varepsilon'_{\omega,\theta}$, are positive at very small scales, as shown in figure 4.

4.4. *Probability distribution of local tracer transfers in the inertial range*

Local transfers at larger scales in the inertial range are related to $F(\boldsymbol{x}, l)$, defined by (2.6). Figure 6 shows the histogram of $F(\boldsymbol{x}, l)$ in elliptic (*a*) and hyperbolic (*b*) regions. $F(\boldsymbol{x}, l)$ is sensitive to the transfer dynamics in the whole inertial range. (Note that, at small scales, the histograms of $F(\boldsymbol{x}, l)$ and σ must be equivalent owing to the small-scale limit (2.7). This property is satisfied in our numerical experiments (results not shown).) The two-point separation is fixed at $6\Delta x$, where Δx is the grid spacing. In terms of non-dimensional length scales, this corresponds to $l/l_I \approx 0.3$, where the elliptic enstrophy transfer is negative (see figure 4).

Figure 6(*a*) shows that elliptic regions are characterized by a more frequent occurrence of negative (inverse) enstrophy transfers. This leads to a negative average of the histogram of enstrophy transfers in elliptic domains and it indicates the presence of a (local) inverse enstrophy cascade in the inertial range. Nothing like this is observed for the passive tracer, which displays a symmetric distribution. On the other hand, vorticity and passive tracer display similar histograms in hyperbolic domains (figure 6*b*). Here, the average is always positive, consistent with a direct (forward) cascade for both active and passive tracers.

4.5. *Identification of the structures responsible for the inverse enstrophy cascade*

The results discussed until now do not allow unambiguous determination of the structures responsible for the anomalous backward enstrophy cascade. Elliptic regions include both vortex cores and vorticity filaments in the background, and at this point it is not clear which of these structures is responsible for the inverse enstrophy cascade. In addition to the selection criterion based on the value of Q^*, we further partition the set of elliptic regions, based on their average squared vorticity. A conditional average of $F(\boldsymbol{x}, l)$ over the domains defined by the double constraint on Q^* and ω^2 gives a new estimate of ε'_{ω}, which must be compared to the global elliptic contribution displayed in figure 4.

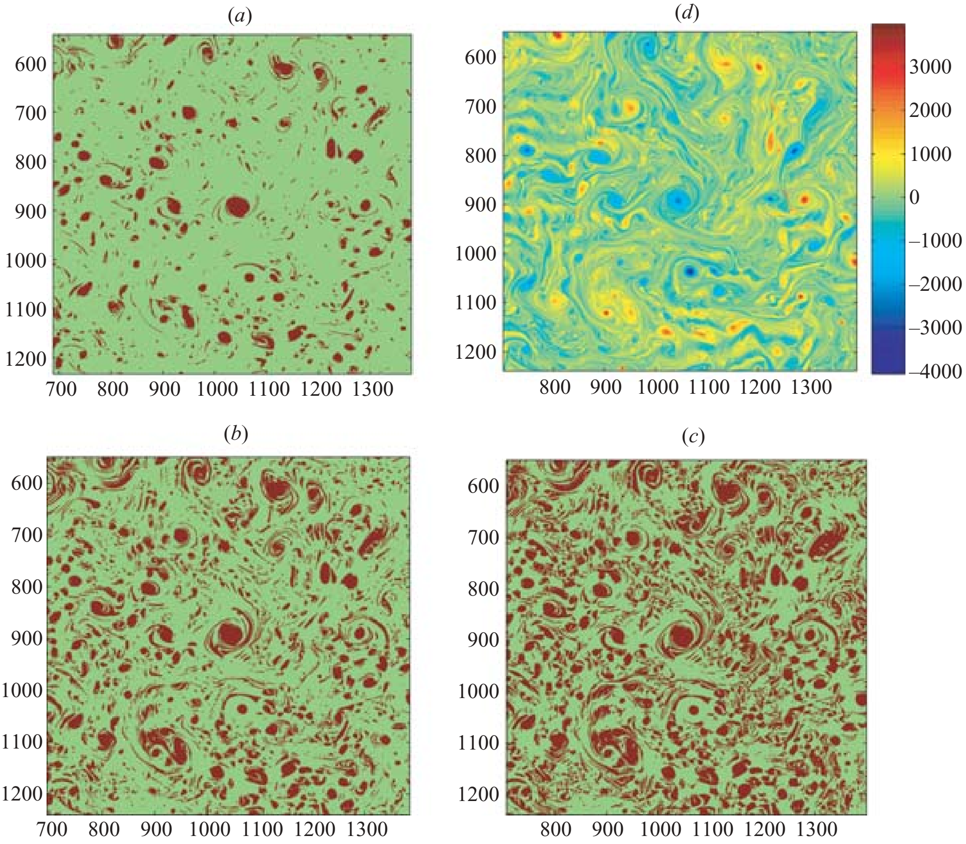

FIGURE 7. Vorticity field (*d*) and spatial distribution of elliptic domains associated with different vorticity levels. (*a*) $Q^* < 0$ and $\omega^2 > 4Z$, (*b*) $Q^* < 0$ and $\omega^2 > Z$, (*c*) $Q^* < 0$.

Figure 7 shows the vorticity field (panel *d*) and the elliptic domains corresponding to different vorticity levels (panels *a*, *b*, *c*). The selection of elliptic domains corresponds to the constraints: (*a*) $Q^*(\boldsymbol{x}) < 0$ and $\omega^2(\boldsymbol{x}) > 4Z$ where Z is the globally averaged enstrophy; (*b*) $Q^*(\boldsymbol{x}) < 0$ and $\omega^2(\boldsymbol{x}) > Z$; and (*c*) all elliptic domains, $Q^*(\boldsymbol{x}) < 0$. Case (*a*) basically captures the cores of the vortices.

The elliptic enstrophy transfers associated with the different domains are shown in figure 8. For the vortex cores (dashed line), the elliptic enstrophy transfers are negative. However, they remain rather small except at length scales of the order of the injection scale l_I, that approximately determines the scale of the larger vortices. As the threshold for ω^2 decreases, the elliptic domains become more fragmented and are composed of clusters of small-scale elliptic patches and vorticity filaments with characteristic size smaller than the vortex size (figure 7*c*). The corresponding elliptic transfers (continuous line in figure 8) become closer to the estimate for the whole set of elliptic regions (circles). This indicates that the main contribution to the anomalous backward enstrophy cascade arises from fragmented elliptic patches and vorticity filaments around and between the coherent vortices.

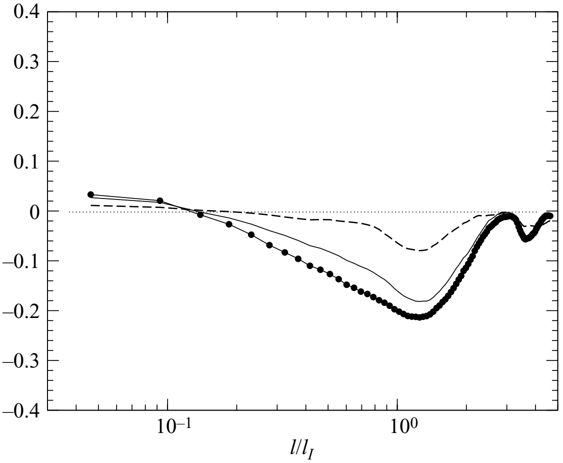

FIGURE 8. Elliptic enstrophy transfers as a function of length scale for the partitioning criteria based on the values of Q^* and ω^2. The circles indicate the case $Q^* < 0$, the continuous line indicates $Q^* < 0$ and $\omega^2 > Z$, and the dashed line indicates $Q^* < 0$ and $\omega^2 > 4Z$, where Z is the globally averaged enstrophy.

5. Links with energy transfers

Clusters of small-scale elliptic patches with same-sign vorticity often participate in aggregation processes that lead to the formation of larger-scale structures (Paret & Tabeling 1998; Babiano & Dubos 2005). As the merging of same-sign coherent vortices is one component of the inverse energy cascade at large scales, we speculate that the aggregation of the small-scale elliptic patches in the enstrophy inertial range is an elementary mechanism of small-scale backward energy cascade. If this picture is correct, then in small-scale clusters of elliptic patches both the energy and the enstrophy cascades are directed towards larger scales. The inverse enstrophy cascade should thus be associated with smoothing of vorticity gradients and growth of larger-scale motions.

5.1. *Elliptic enstrophy transfer and gradient-decreasing processes*

First we need to verify whether inverse enstrophy transfers in elliptic regions are associated with smoothing of vorticity gradients. To this end, we compare the mean conditional scale-to-scale transfers, $\varepsilon'_\omega(Q^*)$ and $\varepsilon'_\theta(Q^*)$, to the sign of the two-point cascade efficiencies $\sigma_l^+$and σ_l^- for different separations in the inertial range.

Figure 9 shows the conditional transfers for the passive tracer (panel *a*) and for vorticity (panel *b*) as a function of Q^*, at different values of the separation scale l. The total transfers, $\varepsilon'_{\omega,\theta}(Q^*)$, at any value of Q^* are defined as the sum of the two contributions corresponding to σ_l^+ and σ_l^-.

In hyperbolic regions ($Q^* > 0$), the total vorticity and passive-tracer transfers are always positive, consistent with a direct cascade towards small scales. The hyperbolic transfers are dominated by the contribution of σ_l^+, and are thus associated with gradient growth. The hyperbolic transfers associated with σ_l^- are approximately zero.

In elliptic regions ($Q^* < 0$), the situation is more complicated. At small scales, elliptic transfers are positive for both vorticity and passive tracer, as expected from the results discussed above. At larger scales, the elliptic transfers for vorticity and passive tracer become different. The total elliptic passive-tracer transfers are approximately zero, whereas elliptic enstrophy transfers grow with the length scales and become

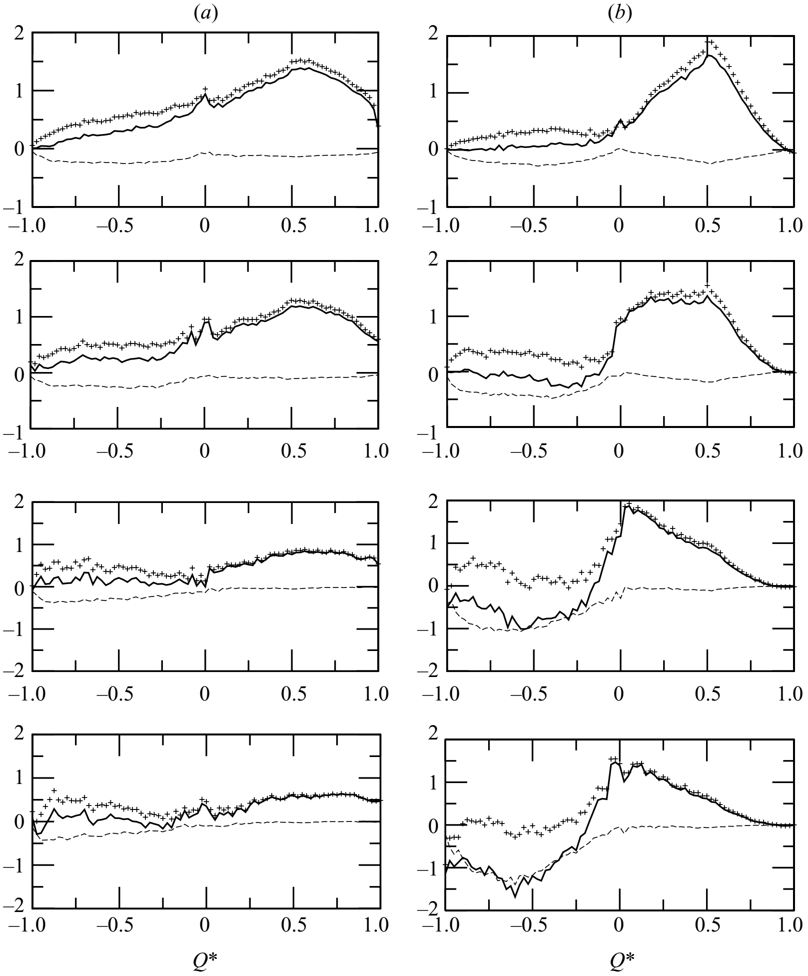

FIGURE 9. Different contributions to tracer transfers as a function of Q^*, for a passive tracer (*a*) and for vorticity (*b*). The continuous line indicates the global transfers, the + symbols indicate the σ^+ contributions and the − symbols indicate the σ^-. From top to botton: $l/\Delta x = 2, 4, 8, 12$, where Δx is the grid spacing.

negative (backward cascade). At the largest length scales analysed, we see that only gradient-decreasing structures characterized by σ_l^- contribute to the elliptic enstrophy transfers. This behaviour is not present in the passive-tracer transfer dynamics. These results confirm that the inverse enstrophy transfers detected in elliptic regions are associated with gradient-decreasing processes.

5.2. *Gradient-decreasing processes and inverse energy transfer*

Figure 10 shows the histograms of the third-order moment of velocity increments, $\langle(\boldsymbol{l}/l\cdot\delta\boldsymbol{u})(\delta\boldsymbol{u}\cdot\delta\boldsymbol{u})\rangle$, computed for σ_l^+ and σ_l^- in elliptic regions where $Q^* < 0$. The sign of the third-order moment of the velocity increments characterizes the direction of energy transfers: the third-order moment is positive for inverse energy transfers and negative for direct energy transfers (Babiano & Dubos 2005).

The histograms shown in figure 10 exhibit opposite asymmetries: the third-order moments of velocity increments associated with σ_l^+ contributions have negative mean

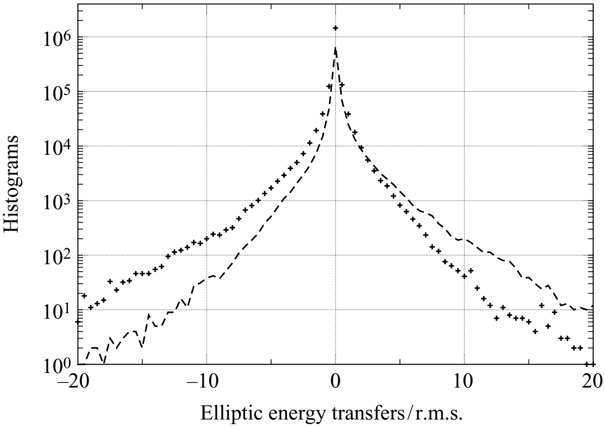

FIGURE 10. Histograms of third-order moments of velocity increments in elliptic regions, for σ_l^+ (+) and σ_l^- (−); $l = 12\Delta x$.

and are characterized by higher efficiency of direct transfers, whereas those associated with σ_l^- contributions are characterized by a positive mean and by the presence of significant inverse transfers towards large scales. Thus, in small-scale elliptic patches there is a close link between smoothing of vorticity gradients (associated with σ_l^-) and backward energy cascades. Conversely, the growth of vorticity gradients is associated with a direct cascade of energy from large to small scales. The behaviour in gradient-decreasing, elliptic regions contradicts the global balance (2.9), as both enstrophy and energy are transferred in the same direction.

In terms of geometrical alignment properties, the above results indicate that in small-scale elliptic patches the two backward cascades should lead to a statistical anticorrelation between $\nabla\omega$ and the stretching direction due to the larger-scale strain field. Unfortunately, a direct estimate of the alignment properties can be difficult, as the limits of the numerical resolution and the application of low-pass filtering precedures can hamper the detection of alignment properties at the filter scale (Protas *et al.* 1999, see also Dubos & Babiano 2002).

5.3. *Link between enstrophy and energy cascades*

As a last step in the analysis, we verify the validity of relationship (2.13) for the global averages and for the conditional averages in the elliptic and hyperbolic domains of the turbulent flow. Figure 11 displays global statistics for the third-order velocity moments, $\langle \delta u_\parallel \delta u_\parallel \delta u_\parallel \rangle$ (continuous line) and $\langle \delta u_\parallel \delta u_\perp \delta u_\perp \rangle$ (dashed line), and for the compensated vorticity increments, $-l^2 \langle \delta\omega^2 \delta u_\parallel \rangle / 16$ (circles). If relationship (2.13) holds, then these quantities should be equal and scale as l^3. Figure 11 shows that for global averages, relationship (2.13) is verified at intermediate scales in the enstrophy cascade range. In terms of global transfer dynamics, this is consistent with a direct enstrophy cascade towards small scales, which is balanced by a scale-dependent inverse energy transfer towards large scales.

Figure 12 shows the mean conditional transfer in elliptic regions, $\varepsilon''_\parallel = \delta u_\parallel \delta u_\parallel \delta u_\parallel / l^3$ (continuous line), $\varepsilon''_\perp = \delta u_\parallel \delta u_\perp \delta u_\perp / l^3$ (dashed line) and $\varepsilon''_\omega = -\delta\omega^2 \delta u_\parallel / (16 l)$ (circles), further constrained on σ_l: panel (a) shows elliptic transfers for σ_l^- and panel (b) for σ_l^+. All quantities have been normalized by the mean transfer rate in the enstrophy inertial range.

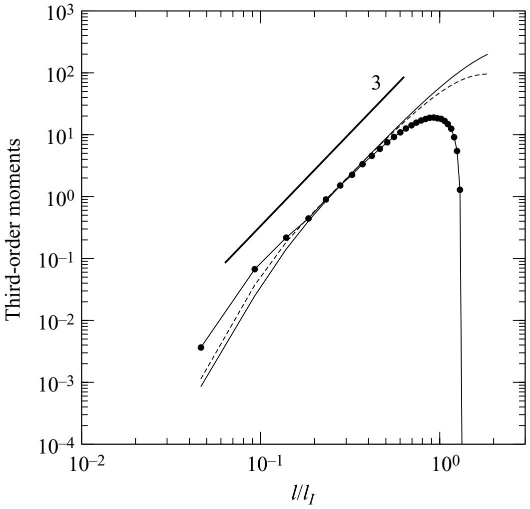

FIGURE 11. Third-order moments of longitudinal (continuous line) and transverse (dashed line) velocity increments and of compensated vorticity increments (circles), as a function of length scale. The thick straight line indicates the l^3 behaviour.

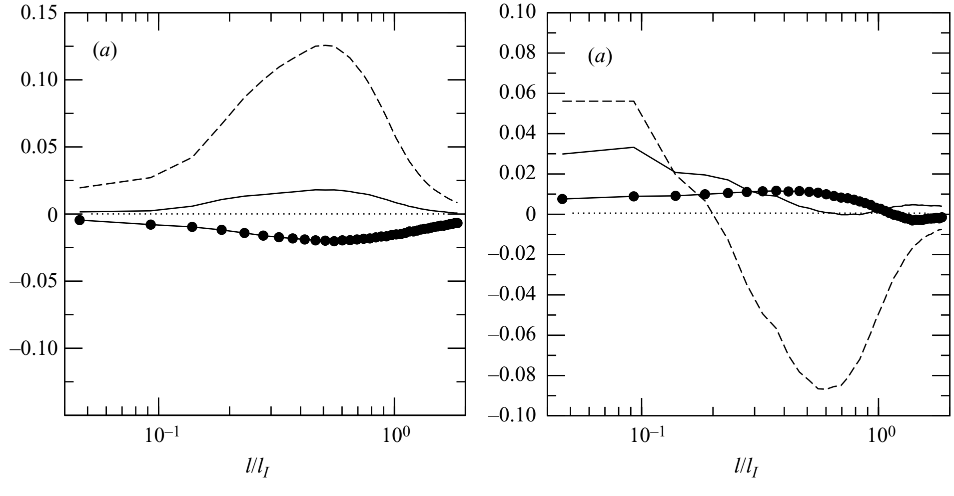

FIGURE 12. Elliptic transfers $\varepsilon''_{\parallel}$ (continuous line), $\varepsilon''_{\perp}$ (dashed line) and ε''_{ω} (circles) as a function of length scale: (*a*) σ_l^-, corresponding to gradient-decreasing regions, (*b*) σ_l^+, corresponding to gradient-increasing regions.

As a first observation, we note a significant difference between $\varepsilon''_{\parallel}$ and $\varepsilon''_{\perp}$ in elliptic domains, compared to their global averages (2.13) shown in figure 11. The magnitude of ε''_{ω} is comparable with that of $\varepsilon''_{\parallel}$, as predicted by the global budget, while it is about 4–5 times smaller than $\varepsilon''_{\perp}$. However, for σ_l^- the sign of ε''_{ω} is opposite to that of $\varepsilon''_{\parallel}$ and $\varepsilon''_{\perp}$.

By virtue of (2.13), the global budget in the enstrophy inertial range is guaranteed by the relationship between the direct enstrophy transfer towards small scales (negative $\langle \delta\omega^2 \delta u_\parallel \rangle/(16l)$) and the inverse energy transfer towards large scales (positive $\langle \delta u_\parallel \delta u_\parallel \delta u_\parallel \rangle/l^3$ and $\langle \delta u_\parallel \delta u_\perp \delta u_\perp \rangle/l^3$). The results shown in figure 12 indicate that this global balance does not hold separately in different topological regions. In elliptic regions characterized by gradient-decreasing structures, both the enstrophy and the energy cascades are inverse. In gradient-increasing regions, the enstrophy cascade is direct, but relation (2.13) does not necessarily hold. Only when globally averaged, do the two cascades obey (2.13).

6. Summary and conclusions

The present work was stimulated by a number of open questions concerning vorticity and passive-tracer dynamics in two-dimensional turbulence. We have reconsidered the main physical features of the enstrophy and passive-tracer cascades and focused on small-scale gradient alignment properties and scale-to-scale enstrophy and tracer-variance transfers in the whole inertial range of the enstrophy cascade. We have quantitatively confirmed and substantiated the suggestion of Ohkitani (1991) on the existence of inverse enstrophy transfers in the elliptic domains of two-dimensional turbulence.

The main results of our numerical exploration can be summarized as follows:

(i) Enstrophy and passive-tracer variance undergo different inertial-range cascade processes in elliptic regions: here, passive-tracer variance goes from large to small scales whereas enstrophy goes from small to large scales. The main contribution to the inverse enstrophy cascade comes from small elliptic patches and vorticity filaments outside coherent vortices. The inversion of the enstrophy cascade in the inertial range is neglected in self-similarity theories and it could explain the fact that the observed enstrophy spectra are steeper than k^{-1}.

(ii) Probability distributions of scale-to-scale transfers in the inertial range show that the dominant contribution to the inverse enstrophy cascade in elliptic domains comes from gradient-decreasing structures.

(iii) The study of third-order moments of velocity increments shows that gradient-decreasing structures in elliptic domains are characterized by inverse energy and enstrophy transfers that do not obey (2.13). On the other hand, this relationship is verified by the global averages.

(iv) At very small scales, both the enstrophy and passive-tracer variance transfers are positive, for both elliptic and hyperbolic regions. This is consistent with gradient growth at the smallest scales in the enstrophy range. This may explain why diagnostics based on local gradient dynamics indicate a similarity of active- and passive-tracer cascades even in elliptic domains.

The inversion of the enstrophy cascade in elliptic, gradient-decreasing patches seems to be the main difference between vorticity and passive-tracer dynamics. As noticed by Ohkitani (1991), the inversion of the enstrophy cascade can be the consequence of the interaction between coherent vortices of size close to the forcing scale, see also Babiano *et al.* (1987). Our results reveal that the inversion of the enstrophy cascade takes place on scales that are definitely smaller than the forcing scale l_I. In our numerical simulations, the inverse enstrophy transfer is especially evident for $l/l_I > 0.2$, a range that corresponds to wavenumbers $k/k_I \leqslant 5$ where the vorticity and passive-tracer spectra have different slopes. The inverse enstrophy transfer taking place in elliptic patches could be one of the basic processes associated with the formation of coherent vortices in forced two-dimensional turbulence.

REFERENCES

Babiano, A., Basdevant, C., Legras, B. & Sadourny, R. 1987 Vorticity and passive scalar dynamics in two-dimensional turbulence. *J. Fluid Mech.* **183**, 379–397.

Babiano, A. & Dubos, T. 2005 On the contribution of coherent vortices to the two-dimensional inverse energy cascade. *J. Fluid Mech.* **529**, 97–115.

Basdevant, C. & Philipovitch, T. 1994 On the validity of the "Weiss criterion" in two-dimensional turbulence. *Physica* D **73**, 17–30.

Batchelor, G. K. 1953 *The Theory of Homogeneous Turbulence*. Cambridge University Press.

Batchelor, G. K. 1959 Small-scale variation of convected quantities like temperature in turbulent fluid. *J. Fluid Mech.* **5**, 113–133.

Batchelor, G. K. 1969 Computation of the energy spectrum in homogeneous two-dimensional turbulence *Phys. Fluids Suppl.* **12**, II 233–133.

Bracco, A., Lacasce, J., Pasquero, C. & Provenzale, A. 2000*a* The velocity distribution of barotropic turbulence. *Phys. Fluids* **12**, 2478–2488.

Bracco, A., McWilliams, J. C., Murante, G., Provenzale, A. & Weiss, J. B. 2000*b* Revisiting freely-decaying two-dimensional turbulence at millennial resolution. *Phys. Fluids* **12**, 2931–2941.

Dubos, T. & Babiano, A. 2002 Two-dimensional cascades and mixing: a physical space apprach. *J. Fluid Mech.* **467**, 81–100.

Dubos, T. & Babiano, A. 2003 Comparing the two-dimensional cascades of vorticity and a passive scalar. *J. Fluid Mech.* **492**, 131–145.

Elhmaidi, D., von Hardenberg, J. & Provenzale, A. 2005 Large-scale dissipation and filament instability in two-dimensional turbulence. *Phys. Rev. Lett.* **95**, 014503.

Elhmaidi, D., Provenzale, A. & Babiano, A. 1993 Elementary topology of two-dimensional turbulence from a Lagrangian viewpoint and single-particle dispersion. *J. Fluid Mech.* **257**, 533–558.

Holloway, G. & Krismannsson, S. S. 1984 Stirring and transport of tracer fields by geostrophic turbulence. *J. Fluid Mech.* **141**, 27–50.

Hua, B. L. & Klein, P. 1998 An exact criterion for the stirring properties of nearly two-dimensional turbulence. *Physica* D **113**, 98–110.

Jullien, M.-C., Castiglione, P. & Tabeling, P. 2000 Experimental observation of Batchelor dispersion of passive tracers. *Phys. Rev. Lett.* **85**, 3636.

Kimura, Y. & Herring, J. R. 2001 Gradient enhancement and filament ejection for a non-uniform elliptic vortex in two-dimensional turbulence. *J. Fluid Mech.* **439**, 43–56.

Klein, P., Hua, B. L. & Lapeyre, G. 2000 Alignment of tracer gradient vectors in two-dimensional turbulence. *Physica* D **146**, 246–260.

Kraichnan, R. H. 1967 Inertial ranges in two-dimensional turbulence. *Phys. Fluids* **10**, 1417–1423.

Landau, L. & Lifshitz, E. 1971 *Mécanique des Fluides*. Édition Mir.

Lapeyre, G., Hua, B. L. & Klein, P. 2001 Dynamics of the orientation of gradients of passive and active scalar in two-dimensional turbulence. *Phys. Fluids* **13**, 251–264.

Lapeyre, G., Klein, P. & Hua, B. L. 1999 Does the tracer gradient align with the strain eigenvectors in 2D turbulence? *Phys. Fluids* **11**, 3729–3737.

Larchevque, M. 1993 Pressure field and coherent structures in two-dimensional incompressible turbulent flows. *Theor. Comput. Fluid Dyn.* **5**, 215–222.

Lesieur, M. & Herring, J. 1985. Diffusion of a passive scalar in two-dimensional turbulence. *J. Fluid Mech.* **161**, 77–95.

Lindborg, E. 1999 Can the atmospheric kinetic energy spestrum be explained by two-dimensional turbulence? *J. Fluid Mech.* **388**, 259–288.

Lindborg, E. & Alvelius, K. 2000 The kinetic energy spectrum of the two-dimensional enstrophy turbulent cascade. *Phys. Fluids* **12**, 945–947.

McWilliams, J. 1984 The emergence of isolated coherent vortices in turbulent flows. *J. Fluid Mech.* **146**, 21–43.

McWilliams, J. 1990 The vortices of two-dimensional turbulence. *J. Fluid Mech.* **219**, 361–385.

Ohkitani, K. 1991 Wave number space dynamics of enstrophy cascade in a forced 2-dimensional turbulence. *Phys. Fluids* A **3**, 1598–1611.

Okubo, A. 1970 Horizontal dispersion of floatable particles in the vicinity of velocity singularities such as convergence. *Deep-Sea Res.* **17**, 445–454.

Paret, J. & Tabeling, P. 1998 Intermittency in the two-dimensional inverse cascade of energy: Experimental observations. *Phys. Fluids* **10**, 3126–3136.

Pasquero, C., Provenzale, A. & Babiano, A. 2001 Parameterization of dispersion in two-dimensional turbulence. *J. Fluid Mech.* **439**, 279–303.

Protas, B., Babiano, A. & Kevlahan, N. K. R. 1999 On geometrical alignment properties of two-dimensional forced turbulence. *Physica* D **128**, 169–179.

Weiss, J. 1991 The dynamics of the enstrophy transfer in two-dimensional turbulence. *Physica* D **48**, 273–294.

Yaglom, A. M. 1949 On the local structure of a temperature field in a turbulent flow. *Dokl. Akad. Nauk. SSSR* **69**, 743.